ACS APPLIED ENERGY MATERIALS

www.acsaem.org
Article

Understanding the Internal Conversion Efficiency of $BiVO_4/SnO_2$ Photoanodes for Solar Water Splitting: An Experimental and Computational Analysis

Laura Geronimo, Catarina G. Ferreira, Valentina Gacha, Dimitrios Raptis, Jordi Martorell, and Carles Ros*

Cite This: ACS Appl. Energy Mater. 2024, 7, 1792−1801
Read Online

ACCESS | Metrics & More | Article Recommendations | Supporting Information

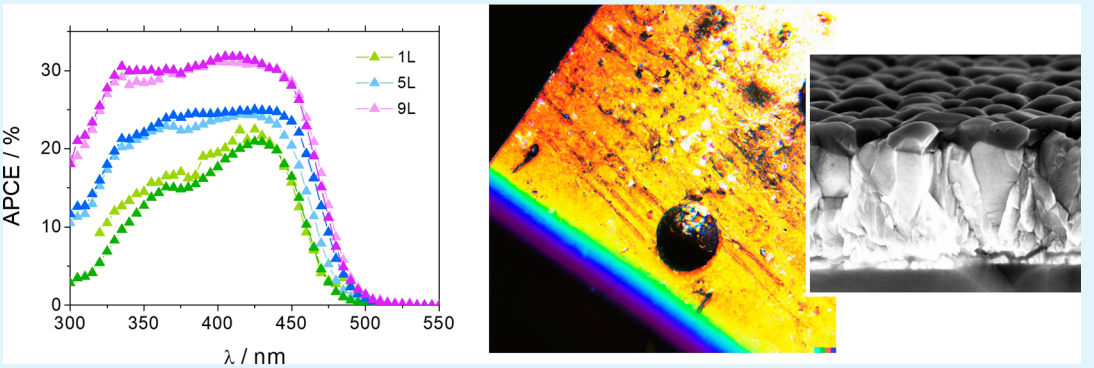

ABSTRACT: This work aims to understand the spin-coating growth process of $BiVO_4$ photoanodes from a photon absorption and conversion perspective. $BiVO_4$ layers with thicknesses ranging from 7 to 48 nm and the role of a thin (<5 nm) SnO_2 hole-blocking layer have been studied. The internal absorbed photon-to-current efficiency (APCE) is found to be nonconstant, following a specific dependence of the internal charge separation and extraction on the increasing thickness. This APCE variation with $BiVO_4$ thickness is key for precise computational simulation of light propagation in $BiVO_4$ based on the transfer matrix method. Results are used for accurate incident photon-to-current efficiency (IPCE) prediction and will help in computational modeling of $BiVO_4$ and other metal oxide photoanodes. This establishes a method to obtain the sample's thickness by knowing its IPCE, accounting for the change in the internal APCE conversion. Moreover, an improvement in fill factor and photogenerated voltage is attributed to the intermediate SnO_2 hole-blocking layer, which was shown to have a negligible optical effect but to enhance charge separation and extraction for the lower energetic wavelengths. A Mott−Schottky analysis was used to confirm a photovoltage shift of 90 mV of the flat-band potential.

KEYWORDS: *$BiVO_4$, spin-coating, water splitting, catalysis, hydrogen*

INTRODUCTION

The increasing urgency to fight against the consequences of climate change, such as global warming, heavy rainfall, or droughts, has led to an exponential increase in research interest in renewable energy sources and, in particular, solar energy. However, despite the high-power conversion efficiencies achieved by photovoltaic cells,[1,2] their operation is limited by daylight hours and ambient conditions. Because of that, there is high interest in developing technologies capable of storing solar energy in the form of molecular fuels. Hydrogen, produced from water splitting, is one of the most promising solar fuels, with high energy density.[3]

The photoelectrochemical (PEC) water splitting process is capable of converting solar energy directly into chemical energy by absorbing photons and generating enough potential to split H_2O molecules.[4] The PEC effect was first discovered on TiO_2,[5] and much research has been done with it,[6,7] but its large band gap (3.2 eV) limits the absorption to ultraviolet light, which accounts for only 4% of the total solar spectrum. Some other metal oxides such as WO_3[8] and Fe_2O_3[9] have also been intensively studied but lack either a shorter band gap or proper carrier mobility.[10]

Bismuth vanadate ($BiVO_4$) is one of the most promising semiconductors for PEC water splitting due to its relatively narrow band gap of 2.4 eV, which allows for a theoretical maximum solar-to-hydrogen conversion efficiency of 9.1%.[4,11]

Received: November 2, 2023
Revised: December 22, 2023
Accepted: February 6, 2024
Published: February 20, 2024

In addition, it is a nontoxic, inexpensive, and earth-abundant material that presents good stability in neutral-alkaline electrolytes.[12] Nevertheless, bismuth vanadate is also known for suffering from high surface recombination of photogenerated electron−hole pairs and poor charge transfer,[13] which results in a short carrier diffusion length (~70 nm).[10,11] This sets a maximum limit for the $BiVO_4$ thickness to avoid significant resistivity but also restricts the photocurrent achievable due to the partial light absorption. In addition, it lacks a surface that is prone to the oxygen evolution reaction. Therefore, extensive research has been conducted on passivating its superficial states and enhancing its catalytic activity. This investigation involves the coordination of electrocatalysts, such as CoPi[14] or NiFeOOH,[15] to augment the material's overall performance.

$BiVO_4$ photoanodes can be fabricated following multiple deposition methods, such as spin-coating,[16] pulsed laser deposition,[12] spray pyrolysis,[17] or electrodeposition,[18] resulting in highly variable performances and film morphologies. Enhancements in the PEC performance of $BiVO_4$ photoanodes are reported by different approaches, such as forming hetero- or semiconductor/electrocatalyst junctions, enabling an improvement of the charge transport and the transfer efficiencies simultaneously.[19] It has been also demonstrated how a proper surface treatment can significantly enhance photocatalytic activity,[20] and adding a charge-blocking layer can reduce surface recombination, resulting in higher photocurrents.[21]

Even so, a single $BiVO_4$ absorber requires an external bias to perform the water splitting reaction, and normally, a wide range of the solar spectrum is lost.[22] A tandem configuration consisting of a photovoltaic/photoelectrode (PV/PEC) device is a good option to overcome these problems,[19,23] but this requires high transmittance for all wavelengths not absorbed by the photoanode and therefore compact non-nanostructured $BiVO_4$ films. This way, the PV cell with band gap energy (E_g) lower than that of the $BiVO_4$ will efficiently absorb the light transmitted from the photoanode and then generate enough voltage to assist the bias-free water splitting reaction.[23] In this context, the most effective $BiVO_4$ synthesis methods are intentionally omitted due to the undesirable highly scattering films they produce.[24−26] Spin-coating, which yields intermediate-performance films characterized by both compactness and transparency, emerges as essential. This method plays a crucial role in the fabrication of compact tandem devices,[23] enabling the realization of bias-free targeted reactions.

This work studies the correlation between photon absorption and internal conversion efficiency and the growth process of $BiVO_4/SnO_2$ thin-film photoanodes. The samples were fabricated by a spin-coating deposition method to ensure a compact thin film with minimal light scattering, which results in a transparent material in the region below the band gap, that can be used in tandem PV/PEC configurations.[23] Light conversion capabilities were studied for varying film thicknesses and the introduction of a SnO_2 hole-blocking layer (HBL). The absorbed photon-to-current efficiency (APCE) was extracted from the experiments, and a correlation of the internal photon conversion rates for different thicknesses was obtained. This allows us to easily obtain one of the quantities (thickness or APCE) just by knowing the other one, at least for the thickness range obtained, for the first time in this study. The identification of this dependency between the internal conversion and the thickness was proven to help optimize the computational simulation of the incident photon-to-current efficiency (IPCE), based on a transfer matrix method, and will help in computational modeling of metal oxide photoanodes.

MATERIALS AND METHODS

Materials. Bismuth(III) nitrate pentahydrate ($Bi(NiO_3)_3{\cdot}5H_2O$, 99.99%), vanadyl acetylacetonate ($C_{10}H_{14}O_5V$, 97%), acetylacetone ($C_5H_8O_2$, 99%), tin(II) chloride dihydrate ($SnCl_2{\cdot}2H_2O$), iron(II) sulfate heptahydrate ($FeSO_4{\cdot}7H_2O$, 99%), nickel(II) sulfate hexahydrate ($NiSO_4{\cdot}6H_2O$, 98%), boric acid (H_3BO_3, 99.5%), potassium hydroxide (KOH, flakes, 90%), sodium sulfite (Na_2SO_3, 98%), zinc acetate dihydrate ($Zn(CH_3COO)_2{\cdot}2H_2O$), ethanolamine ($NH_2(CH_2)_2OH$), 2-methoxyethanol ($CH_3O(CH_2)_2OH$), and 1-chloronaphthalene ($C_{10}H_7Cl$) were all purchased from Sigma-Aldrich. Fluorine-doped tin oxide substrates (FTO glasses, 5 cm × 5 cm), with a sheet resistance of 15 $\Omega{\cdot}cm^{-2}$, were obtained from Sigma-Aldrich.

Preparation of the $BiVO_4$ Photoanodes. $BiVO_4$ films were prepared on top of previously cleaned FTO-coated glass substrates using a layer-by-layer spin-coating deposition method. To fabricate the final bismuth vanadate solution, two precursor solutions of 0.2 M of $Bi(NO_3)_3{\cdot}5H_2O$ and 0.03 M of $C_{10}H_{14}O_5V$, both dissolved on acetylacetone, were mixed and sonicated for 15 min before and after the mixing. To get each layer, 20 μL of $BiVO_4$ solution was spin-coated (Laurell Technology) twice in a row at 1000 rpm for 10 s, with an acceleration rate of 250 $rpm{\cdot}s^{-1}$, followed by a treatment in an oven at 500 °C in air for 5 min, for precrystallization. This process was repeated for 1, 5, and 9 layers, after which final annealing at 500 °C was performed for 2 h at a heating rate of 15 $°C{\cdot}min^{-1}$, for complete crystallization.

A SnO_2 solution with a concentration of 30 μM was prepared from $SnCl_2{\cdot}2H_2O$ using isopropanol as the solvent, stirred for 5 h, and aged for 24 h at room temperature to increase its viscosity. The SnO_2 layer was also deposited by spin-coating on top of some of the FTO substrates at 2000 rpm for 30 s.

$BiVO_4$ photoanodes composed of 1, 5, and 9 spin-coating layers were fabricated both directly on top of bare FTO/glass and on substrates coated by a thin layer of SnO_2. Bare FTO samples with and without the addition of a thin layer of SnO_2 were made as references and equally studied.

Morphological and Optical Measurements. Samples' morphological, cross-sectional, and grain size analyses were made using a Zeiss series Auriga FIB-SEM microscope operated at 5 kV. UV−vis measurements were performed with a PerkinElmer Lambda 950 UV/vis spectrometer, from which we obtained both specular transmittance and reflectance in a range from 300 to 800 nm, in steps of 5 nm. To estimate the band gap from the UV−vis data, Tauc's[27] direct and indirect band gap equation was applied.

Photoelectrochemical Measurements. Photoelectrochemical measurements were performed by using a 7 mL single-compartment cell with a 0.5 cm^2 circular window. All the PEC measurements were performed under back-side illumination in a three-electrode setup made up of a Pt counter electrode (CH Instruments CHI115), a 1.0 M potassium chloride (KCl) Ag/AgCl reference electrode (CH Instruments CHI111), and the $BiVO_4$ photoanode as the working electrode, the potential being controlled by a BioLogic SP-300 potentiostat. A 1.0 M potassium borate (KBi) solution, with pH corrected to pH 9 by the introduction of potassium hydroxide (KOH), and with the addition of 0.5 M sodium sulfide (Na_2SO_3) as a hole scavenger, was used as an electrolyte for the water splitting reaction.

Cyclic voltammetry measurements were performed under simulated AM 1.5G solar illumination (100 $mW{\cdot}cm^{-2}$) from a solar simulator (Sun 2000 class A, Abet Technologies), with a scan rate of 50.0 $mV{\cdot}s^{-1}$. Values of the series (R_s) and shunt resistance (R_{sh}) are determined as the inverse of the slope of the linear regions on the $j-V$ curves at low (0.4−0.5 V_{RHE}) and high (1.23 V_{RHE}) applied potentials, respectively. The onset potential (V_{on}) is defined at 0.01 $mA{\cdot}cm^{-2}$ photocurrent density (average of the forward and reverse scans), and the photogenerated voltage (V_{ph}) is calculated as the potential

https://doi.org/10.1021/acsaem.3c02775
ACS Appl. Energy Mater. 2024, 7, 1792−1801

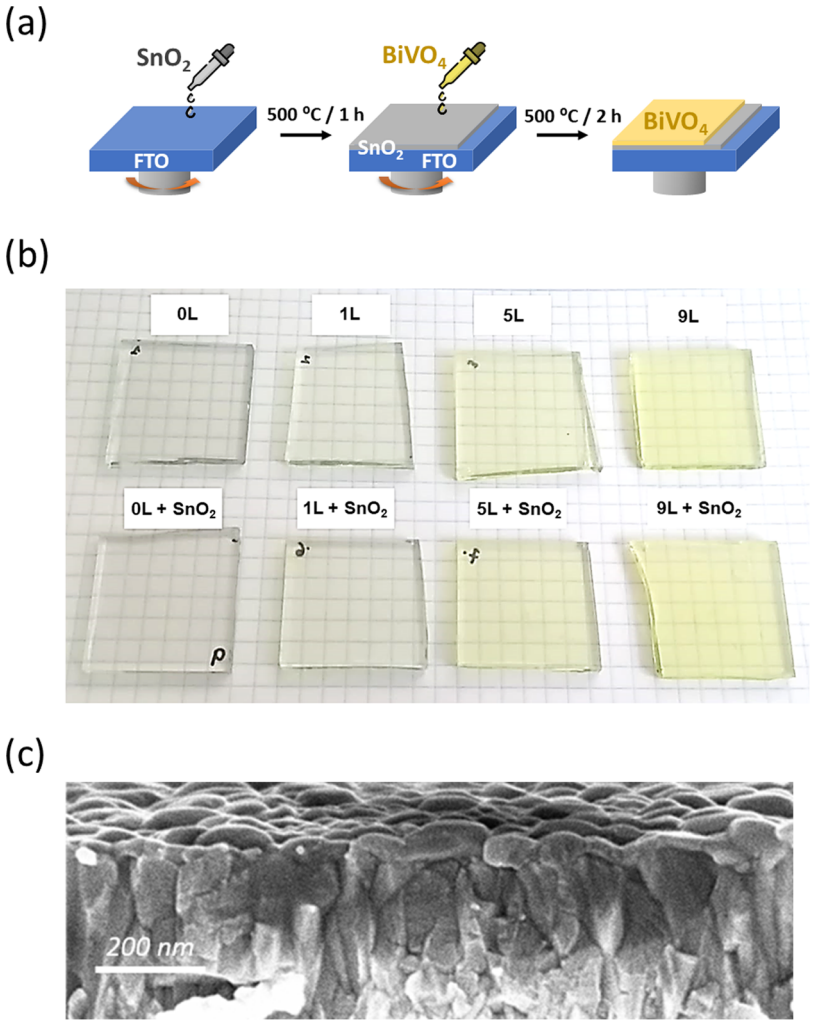

Figure 1. (a) Schematic representation of the spin-coating process used to deposit the $BiVO_4$ photoanodes on top of FTO/glass substrates. (b) Samples used in the experiments were classified by the number of deposited $BiVO_4$ layers and the presence or absence of SnO_2. (c) Cross-sectional SEM micrograph of the 9-layer $BiVO_4$ + SnO_2 sample.

between V_{on} and 1.23 V_{RHE}. IPCE measurements were carried out in the same three-electrode configuration, at a fixed potential of 1.23 V_{RHE}, using a monochromator (Oriel 260 Cornerstone, Newport Instruments) illuminated with a 300 W xenon lamp (OPS-A500, Newport) and incorporating additional automated long-pass filters to cut out more energetic second-harmonic photons from the grating. To calculate the IPCE values from the experimental data collected, the following relation was used[28]

$$\text{IPCE}\ (\%) = \frac{1240 \times J_{ph}(\lambda)}{\lambda \times P_{inc}(\lambda)} \times 100 \tag{1}$$

where $J_{ph}(\lambda)$ is the measured photocurrent density ($mA{\cdot}cm^{-2}$) and P_{inc} is the incident light power density ($W{\cdot}cm^{-2}$) for each wavelength considered, which was recorded with a calibrated S120VC photodiode (Thorlabs). The APCE was calculated as the ratio between IPCE and 1-T-R.

Mott−Schottky plots are obtained with the same photoelectrochemical conditions and equipment, and the relation between the capacitance of the space charge layer, the doping level, and the applied potential is obtained by the following equations[29]

$$\frac{1}{C_{sc}^2} = \frac{2}{\epsilon\epsilon_0 A^2 q N_D}\left(V - V_{fb} - \frac{kT}{q}\right) \tag{2}$$

$$W = \frac{2\epsilon\epsilon_0(V_{mpp} - V_{fb})}{qN_D} \tag{3}$$

where ϵ_r is the relative permittivity of the semiconductor material (for $BiVO_4$ ~ 86[30]), ϵ_0 is the permittivity at vacuum ($\epsilon_0 = 8.854 \times 10^{-14}$ $F{\cdot}cm^{-1}$), q is the charge of an electron, k is the Boltzmann constant ($\frac{kT}{q} \sim 25.0$ mV), V_{MPP} is the voltage at maximum power, and N_D is the donor density.

Computational Simulations. A transfer matrix approach, combining light incoherence at the thick glass substrate with coherence at the FTO/$BiVO_4$ thin-layer stack, was considered to describe light propagation at the photoanode, which was assumed to be composed of flat layers, all parallel to each other.[31,32] Refractive indexes of the different materials were determined by ellipsometry measurements. To estimate the thickness of the $BiVO_4$ layer for the different photoanodes, a least means square method was used in combination with the transfer matrix approach to fit the experimental data for the transmittance and specular reflectance. Simulated IPCE curves were obtained by considering these estimated thicknesses together with the APCE values extracted experimentally.

RESULTS AND DISCUSSION

In this work, $BiVO_4$ photoanodes were deposited on top of FTO/glass substrates, with and without the addition of a thin SnO_2 hole-blocking layer, using a layer-by-layer spin-coating

https://doi.org/10.1021/acsaem.3c02775
ACS Appl. Energy Mater. 2024, 7, 1792−1801

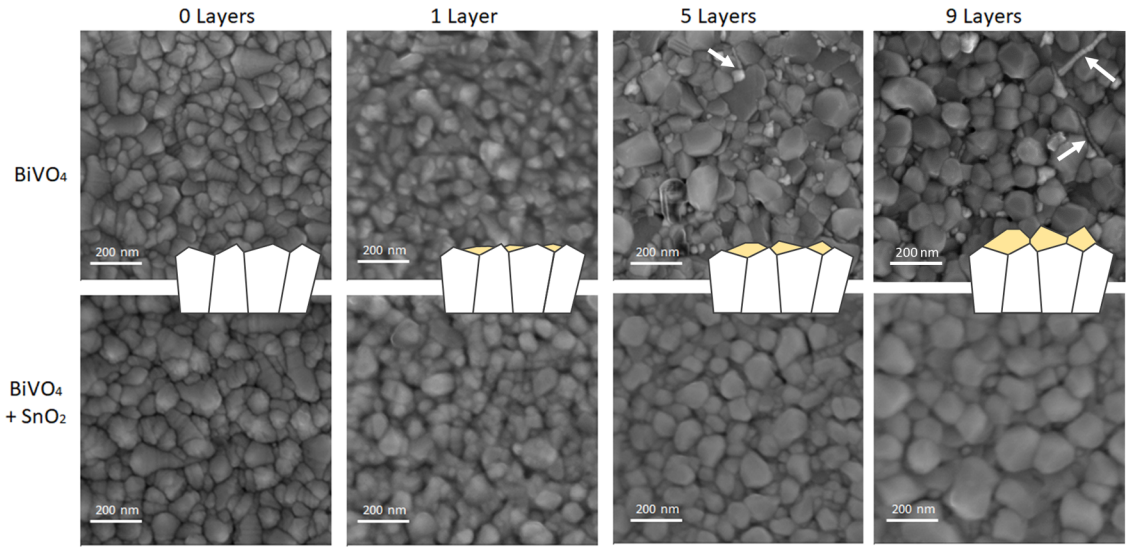

Figure 2. Top-view SEM micrographs of $BiVO_4$ and $BiVO_4$ + SnO_2 thin films with different numbers of layers. A scheme of the $BiVO_4$ crystal development is included. Exposed FTO features are indicated with white arrows.

deposition technique, schematically illustrated in Figure 1a and explained in more detail in the Materials and Methods section of this manuscript. To study the growth process of the $BiVO_4$ and the influence of its thickness in terms of photoactivity of the photoanodes, different samples composed of 0, 1, 5, and 9 spin-coating layers of bismuth vanadate were deposited both on FTO/glass and on SnO_2/FTO/glass substrates. The final samples obtained are pictured in Figure 1b, together with the nomenclature used to address them in this document. As clearly illustrated in this figure, the samples become more yellowish with the addition of $BiVO_4$ layers, but they maintain high transparency regardless of the number of layers considered, which makes them very suitable for tandem photoanode−photovoltaic applications. At the nanoscale, a granular film is formed on top of the FTO polycrystalline film on a glass substrate, as shown in Figure 1c. The inclusion of additional spin-coating layers (>10L) induces a dewetting process in the $BiVO_4$ film. This leads to the agglomeration of the material into large particles, resulting in pronounced scattering and, thus, minimal transmittance (Figure S1). Consequently, this hinders the applicability of these samples in tandem structures, a crucial consideration within the specific context of this study. Based on that, we limited the study to a maximum of 9 spin-coated layers.

Morphological Characterization. Morphological characterization of the different $BiVO_4$ photoanodes was carried out by SEM analysis. The cross-sectional SEM micrograph of a 9-layer sample deposited on top of SnO_2/FTO/glass is presented in Figure 1c and reveals that the $BiVO_4$ has grown as a compact, homogeneously distributed grain film, without any signs of a multilayer deposition. This indicates that the final 2 h annealing treatment, performed on all samples, has probably resulted in a reorganization of the precrystallized films. The average layer thickness for this 9-layer $BiVO_4$ sample was estimated from the SEM cross-sectional analysis to be 48 nm, as demonstrated in Figure S2. In addition, no signs of the SnO_2 layer were detected, which indicates that its thickness may be lower than the cross-sectional SEM resolution (<5 nm).

Figure 2 shows the top-view SEM micrographs for all eight samples with an increasing number of $BiVO_4$ layers in the presence or absence of a thin SnO_2 layer. The first thing we observed from the analysis of these images was that the samples that contain one layer of SnO_2 appear slightly blurrier than the ones with just $BiVO_4$. This can have two main explanations: the photoanodes have slightly less conductivity than when in direct contact with FTO, which influences SEM resolution by slightly deflecting the electrons, or films have become smoother with the addition of a small SnO_2 layer, as it was seen in some recent studies.[21,33]

Despite that, for the same number of $BiVO_4$ layers, the film morphology seems to be quite similar regardless of the presence of the SnO_2 hole-blocking layer. In particular, when a single layer was deposited, top-view analysis resembled the one of the bare FTO/glass substrates but with blurrier grain boundaries. When the number of layers was increased to 5 and 9, rounded $BiVO_4$ grains started to be visible and to cover the FTO surface. However, only partial coverage of the substrates was achieved in both cases, with multiple rounded grains of $BiVO_4$ growing separated from each other and exposing the FTO grains beneath. So, it seems that the FTO rugosity is filled with $BiVO_4$ grains, and the tips of the FTO's tallest grains are more likely to be exposed. It can be seen how specific features of the FTO substrates, such as elongated grains (probably FTO grains with a specific crystallographic orientation), are found exposed more often than smaller rounded grains, suggesting that it is more difficult for $BiVO_4$ to grow on top of these FTO crystalline orientations. This means that the underlying substrate will be exposed to the electrolyte.

Grain sizes of the different $BiVO_4$ films, extracted from the analysis of the SEM micrographs, progressively increased with the addition of more layers. As shown in Figure 2 and the histograms of grain size in Figures S3 and S4, the average grain diameter goes from ∼85 nm for the 5-layer $BiVO_4$ samples, up to 98 nm, for the 9-layer photoanodes, and it is not affected by the presence of SnO_2. As commented previously, $BiVO_4$ grains are not distinguishable in the 1-layer samples. Some previous works have reported that the SnO_2 thickness, when higher than 40 nm, has a role in the $BiVO_4$ crystallization.[21] In our case, however, the hole-blocking layer is much thinner than that, which explains why the presence of SnO_2 does not influence the growth of the $BiVO_4$ grains. Moreover, the average film thickness of the 9-layer photoanode is about half the average

https://doi.org/10.1021/acsaem.3c02775
ACS Appl. Energy Mater. 2024, 7, 1792−1801

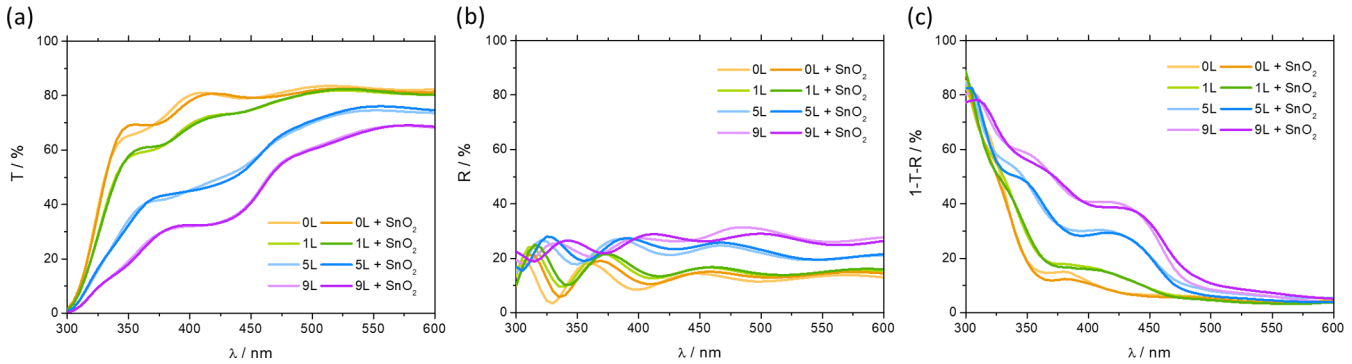

Figure 3. UV−visible (a) transmittance (T) and (b) reflectance (R) and (c) 1-R-T spectra of the fabricated $BiVO_4$ photoanodes with and without SnO_2.

grain width, which suggests a good contact between the $BiVO_4$ film and the FTO and a favorable chemical surface tension during the thermal crystallization process at 500 °C.

Different grain sizes and grain orientations can have a significant effect as this can lead to a high number of structural defects that can act as carrier traps and recombination centers, leading to lower photoelectrochemical activity,[14] or favor $BiVO_4$ growing with some preferential crystalline orientation.[16,34]

Optical Characterization. UV−visible specular transmittance (T) and reflectance (R) measurements were obtained for the fabricated samples (Figure 3a,b). T values are observed to have a significant reduction for wavelengths <350 nm, directly related to the absorption of the FTO substrate, while wavelengths in the 350−550 nm range are less transmitted when increasing the amount of $BiVO_4$ layers. Meanwhile, R values stay in the range of 15−30% for all wavelengths. SnO_2 has no significant role in either T or R. With these, 1-T-R can be calculated (Figure 3c) and represents the wavelengths absorbed or scattered by the sample. 1-T-R values are observed to be directly correlated to the number of deposited layers (Figure 3) and, thus, the optical path through the material. By observing the sample's 1-T-R spectra, it can be affirmed that both the bare $BiVO_4$ samples and the ones having a SnO_2 interlayer have similar absorption values and profile, meaning that $BiVO_4$ thickness is very similar independently of the presence of SnO_2 and that the latter has a minimal optical role.

There is an onset near 470 nm, red-shifted when increasing the number of $BiVO_4$ layers, and the 1-T-R values significantly increase for more energetic photons. The 330−470 nm region appears to be dominated by the absorbance of the $BiVO_4$ deposited film, reaching 1-T-R values up to 60% for 9 layers. It presents two increasingly undulated steps that can be attributed to light interference on a different dielectric constant multilayer stack ($BiVO_4$/SnO_2/FTO/Glass). Meanwhile, in the 330−300 nm region, samples present 60−80% 1-T-R values, similar to bare FTO/Glass. For wavelengths greater than 470 nm, below the $BiVO_4$ band gap energy, samples present non-negligible 1-T-R values. This can be explained by nonzero diffuse reflectance and transmittance light dispersion, not accounted for in 1-T-R, and by the presence of a tail of absorption states, probably due to imperfections in the $BiVO_4$ crystallographic structure.[35] Results obtained by the interpolation of the linear region following the Tauc plot based on the direct band gap case (Figure S5a) reveal band gaps in the range of 2.61−2.72 eV with increasing thickness, regardless of the inclusion of the SnO_2 hole-blocking layer, which agrees with other reported values.[19,36] The indirect band gap (Figure S5b) points at slightly smaller values (2.55 to 2.67 eV), although its determination is difficult due to light scattering and point defects in the photoanode.[36−38]

(Photo)electrochemical Characterization. Cyclic voltammetries, in a three-electrode system, obtained for the herein studied samples at dark and under back illumination are displayed in Figures S5, S6 and Figure 4, respectively. Using back-side illumination has positive implications on the PEC performance of materials that have bad carrier transport, such as $BiVO_4$, because electrons can be directly injected from $BiVO_4$ to the back FTO contact.[39]

Table 1 summarizes typical $j-V$ parameters of the fabricated photoanodes obtained in a way similar to a photovoltaic device curve. Both an increase in photocurrent density at 1.23 V_{RHE} and a cathodic shift of the onset potential of the photoanodes are observed when adding $BiVO_4$ layers. In particular, the 9-layer bare $BiVO_4$ sample presents the highest photocurrent density at 1.23 V_{RHE}, of 0.72 mA·cm^{-2}, which is in the same order as other works for 40 nm thick layers.[39] There is a small improvement in the short-circuit photocurrent density at 1.23 V_{RHE} by the presence of SnO_2, for any number of $BiVO_4$ layers considered, but we can see a major effect of the SnO_2 layer when looking at the profile of the curves: a better photodiode shape is obtained, with higher photocurrents obtained at similar potentials, together with lower hysteresis. These observations are in correlation with the electrical parameters determined with the addition of a SnO_2 layer (Table 1): onset values of the potential are cathodically shifted compared to the samples with bare $BiVO_4$, especially if we look at the 5- and 9-layered samples, which implies higher photogenerated voltage (V_{ph}) for these photoanodes and also an observable cathodic shift of the potential at the maximum power point (V_{mpp}), to about 70 mV. In addition, a combined increase of the shunt resistance (R_{sh}) and a decrease in series resistance (R_s) with the addition of the SnO_2 layer are registered, which results in a higher fill factor, clearly observed in the $j-V$ curves of Figure 4a. All of these results point to SnO_2 properly acting as a hole-blocking layer (HBL). Samples presenting a higher fill factor will be capable of extracting more power from the photo-absorbed light, thus enabling higher productivity in both single absorber and tandem PEC/PV devices.[40]

The $j-V$ curves under dark conditions, displayed in Figure S6, reveal an anodic current appearing at a high anodic potential in the absence of the SnO_2 layer, which is partially blocked by increasing the number of $BiVO_4$ layers. This means that, without light, the semiconductor acts as a blocking diode,

https://doi.org/10.1021/acsaem.3c02775
ACS Appl. Energy Mater. 2024, 7, 1792−1801

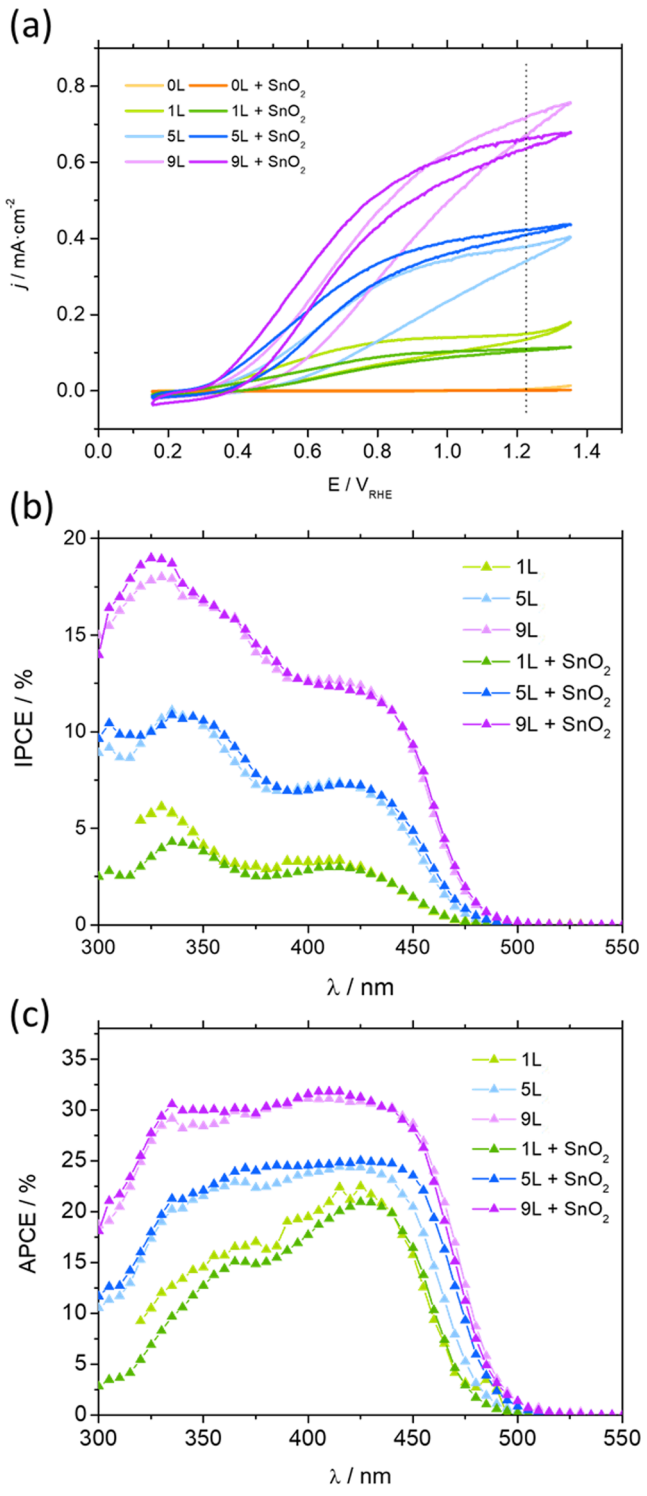

Figure 4. (a) Cyclic voltammetry curves recorded in a three-electrode configuration using an aqueous solution of 1 M KBi with 0.5 M Na_2SO_3 as a hole scavenger (pH = 9) as the electrolyte, with a scan rate of 50.0 mV·s^{-1}, under back-side simulated solar light illumination conditions (AM 1.5 G, 100 mW·cm^{-2}) for 0-, 1-, 5-, and 9-layered $BiVO_4$, with and without the addition of a SnO_2 hole-blocking layer. (b) IPCE spectra of the same samples, measured in a similar configuration, using monochromatic illumination at 1.23 V_{RHE} applied potential. (c) Calculated APCE conversion efficiencies for all samples based on 1-T-R (Figure 3c) and IPCE (Figure 4 b).

preventing electrons coming from the polarized substrate from oxidizing the electrolyte. This is eliminated with the introduction of a SnO_2 layer, which points in the direction of SnO_2 to introduce an enhanced electrical barrier.

Photon-to-Current Efficiency Characterization. The IPCE is a powerful technique to precisely characterize the response of a sample to incident light, independently of the light source.[28] This is especially key in a field such as photoelectrochemistry, where experimental standardization of the conditions is less implemented compared to photovoltaics.[41]

As shown in Figure 4b, higher conversion efficiencies for the whole range of wavelengths are observed for an increasing number of $BiVO_4$ layers, directly in accordance with the photocurrent density at 1.23 V_{RHE} extracted from the $j-V$ profiles of Figure 4a and with the undulated-like 1-T-R profile seen in Figure 3a. Nevertheless, if we compare each photoanode's IPCE divided by the number of layers #L (Figure S7), we observe that the deposition of the first layer of $BiVO_4$ results in the highest IPCE/#L ratio response (6%/L), triple the addition of subsequent layers (2%/L), which maintain a constant increment. This initial divergence is caused by the first $BiVO_4$ layer being deposited directly on the rough surface of the FTO, filling its roughness depths. These depths capture more material during the spin-coating process, resulting in a thicker layer during the first deposition and consequently a higher IPCE/#L due to a longer optical path in the first layer. Increasing to 5 and 9 layers does not change the IPCE/#L ratio, meaning that after the first layer, each spin-coating cycle deposits the same amount of material. A slightly smaller IPCE/#L for the 1-layer $BiVO_4$ + SnO_2 sample points out that the surface has been slightly smoothed previously by the SnO_2 < 5 nm film, as also indicated by the SEM micrographs of Figure 2.

In Figure S8, we also show the IPCE measurements of bare FTO and FTO/SnO_2 substrates, presenting photon conversion for wavelengths in the 300−350 nm range (maximum of 0.05 and 0.25% at 300 nm for FTO and SnO_2, respectively), corresponding to ∼3.50 eV, the band gap of SnO_2,[33] together with a tail of states down to 370−380 nm. This proves that FTO is not a completely degenerately doped metal oxide, presenting slight band bending capable of converting photons into current when in contact with water. The additional SnO_2 thin film significantly increases the conversion capability, caused by the lower doping level compared with FTO.[42]

To better understand the IPCE curves, they must be compared to the 1-R-T measurements. This way, the transmitted, reflected, absorbed, and finally converted photons can be distinguished (Figure S9a−c). These last ones are described by the APCE, presented for every sample in Figure 4c. APCE reveals the internal conversion capability of the absorbent materials themselves, independent of the optical system used. As we have already seen in the Optical Characterization section, our samples present two light absorbance-increasing undulated steps, also visible in the IPCE curves (Figures 3a and 4b), but not in the APCE, meaning that these features were mainly optical. APCE presents three different regions: (1) The 300−330 nm one, dominated by a strong reduction of the conversion capability, caused by photons being first absorbed by the glass, FTO, and SnO_2 layers. With thinner $BiVO_4$ films (more separated $BiVO_4$ nanoparticles, Figure 2), it will be less probable for higher energetic (small wavelengths) photons to interact with the

https://doi.org/10.1021/acsaem.3c02775
ACS Appl. Energy Mater. 2024, 7, 1792−1801

Table 1. Parameters Calculated from the Cyclic Voltammetries Presented in Figure 4a[a]

layers (#)	$j_{1.23VRHE}$ (mA cm^{-2})	R_{sh} (kΩ)	R_s (kΩ)	V_{on} (V_{RHE})	V_{mpp} (V_{RHE})	V_{ph} (V)
			$BiVO_4$			
1	0.148	56.0	6.82	0.40	0.73	0.83
5	0.379	14.4	2.87	0.41	0.77	0.82
9	0.719	5.8	1.77	0.38	0.78	0.85
			$BiVO_4$ + SnO_2			
1	0.110	55.0	5.54	0.41	0.68	0.82
5	0.423	14.9	1.33	0.34	0.72	0.89
9	0.662	6.6	0.82	0.35	0.71	0.88

[a]Short-circuit current density at 1.23 V_{RHE} ($j_{1.23VRHE}$), shunt resistance (R_{sh}), series resistance (R_s), onset potential (V_{on}), potential at maximum power point (V_{mpp}), and photogenerated voltage (V_{ph}), defined as 1.23 V_{RHE}−V_{on}.

$BiVO_4$ nanoparticles, thus missing them; (2) the 350−450 nm one, with a relatively constant conversion rate over wavelengths, especially for a higher number of $BiVO_4$ layers, with 19, 24, and 31% APCE at 400 nm for 1-, 5-, and 9-layer $BiVO_4$ samples, respectively. The increase of internal conversion with thickness must be attributed to the increase of $BiVO_4$'s grain size, allowing for larger band bending[6] and thus better charge separation and extraction, which translates into larger photocurrents; and (3) the 450−500 nm one, corresponding to the absorption edge of $BiVO_4$, which is shifted to lower energies with the increase in $BiVO_4$ thickness.

Thickness Estimation and IPCE Simulation. To better understand and also to predict the PEC behavior of the different $BiVO_4$ samples, computer simulations were performed in which a transfer matrix formalism was employed to describe the light propagation inside the photoanodes. This method is very accurate in describing multilayer systems in which the layers are all flat and parallel to each other and their thicknesses are in the order of the wavelength of the incident light,[31,32] as is the case of the compact $BiVO_4$ photoanodes herein fabricated.

The refractive indexes considered for the FTO and $BiVO_4$ layers are presented in Figure S10. The SnO_2 layer was not included in the simulations, as its thickness is very small and its optical role was found to be irrelevant, as demonstrated in Figure 3.

Using these refractive indexes, the thicknesses of the different photoanodes prepared were estimated by fitting the transmittance and reflectance spectra experimentally measured. The best fits obtained are shown in Figure S11, and according to the results, thicknesses of 7, 23, and 48 nm were estimated for the 1-, 5-, and 9-layer $BiVO_4$ samples, respectively. This agrees with the values extracted from the cross-sectional SEM analysis of Figure 1c, for the case of the 9-layer sample, and it is also in accordance with our prior observations that the first layer deposited is thicker than the remaining ones.

To estimate the IPCE response of the photoanodes, both the thickness of $BiVO_4$ and the absorbed photon-to-current efficiency must be used as input for the computational simulations. Interestingly, as observed in Figure 5a, the APCE values experimentally determined at 400 nm seem to follow a linear trend with the thickness of the $BiVO_4$ layer. This allows us to easily obtain one of the quantities (thickness or APCE) just by knowing the other, at least for the thickness range obtained in this study.

The IPCE curves simulated using the transfer matrix model for a different number of $BiVO_4$ layers are plotted in Figure 5b, together with the experimental responses obtained for the same cases, both with and without the addition of the SnO_2 hole-blocking layer. A good agreement between experimental and simulated curves was obtained, and only small differences in the absorption onset position are observed, which can be

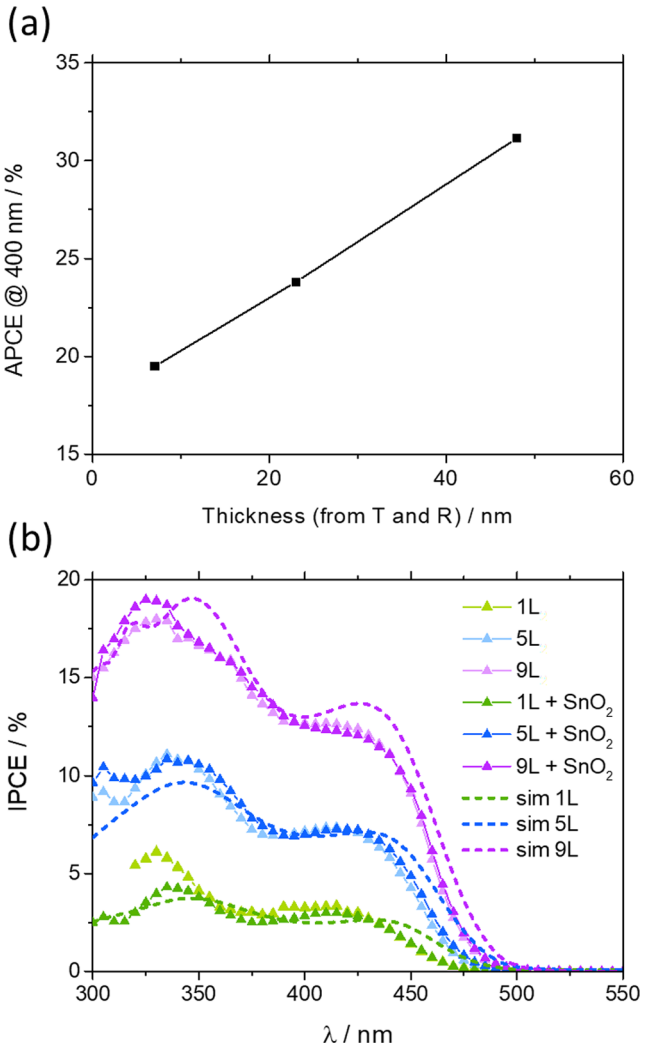

Figure 5. (a) APCE values at 400 nm wavelengths, from Figure 4c, as a function of the thickness simulated from the T and R measurements, where an almost linear correlation can be easily seen. (b) Simulated IPCE (dashed line) overlapped to the experimental IPCE for all samples, fitted with thicknesses of 7, 23, and 48 nm. IPCE was acquired in a three-electrode configuration, using an aqueous solution of 1 M KBi with 0.5 M Na_2SO_3 as a hole scavenger (pH = 9) as the electrolyte, using monochromatic illumination at 1.23 V_{RHE} applied potential.

https://doi.org/10.1021/acsaem.3c02775
ACS Appl. Energy Mater. 2024, 7, 1792−1801

attributed to slight differences between the refractive indexes considered for the $BiVO_4$ absorbing layer and real ones. This shows that it is possible to estimate the sample thickness just by knowing its IPCE, provided that the samples are fabricated following an equal synthesis process.

Role of the SnO_2 Interlayer. Finally, voltage-dependent IPCE and Mott−Schottky (M−S) plots were acquired to understand the role of the SnO_2 intermediate layer. Figure 6a presents the variation of the normalized IPCE spectra upon applied potential. As can be seen, both the 9L and the 9L + SnO_2 samples present almost identical IPCE profiles down to 0.4 V_{RHE}, similar to the ones presented in Figure 4b. The main difference is the capacity of the sample having the intermediate SnO_2 layer to extract more efficiently the photons in the 350−450 nm range. This directly points at the SnO_2 layer helping to increase the electron−hole separation and transport closer to the $BiVO_4$/FTO interface, a larger penetration depth where lower energy photons have more probability to be absorbed.

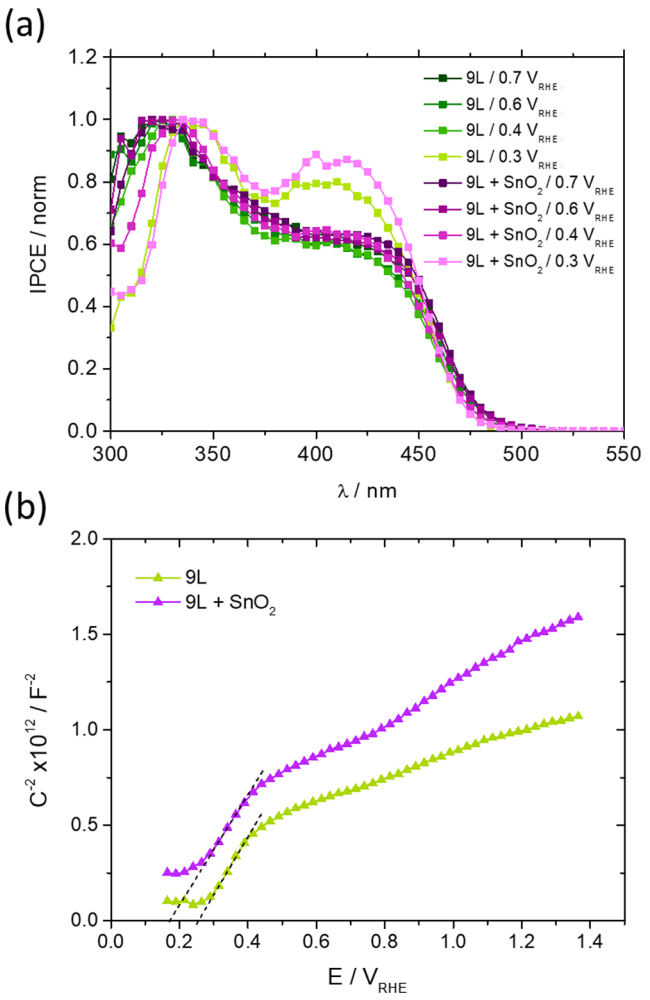

Figure 6. (a) Normalized IPCE measurements of 9L samples, with and without the SnO_2 interlayer, as a function of the applied potential, from 0.7 to 0.3 V_{RHE}. IPCE was acquired in a three-electrode configuration, using an aqueous solution of 1 M KBi with 0.5 M Na_2SO_3 as a hole scavenger (pH = 9) as the electrolyte, using monochromatic illumination. (b) Mott−Schottky plots of nine-layer $BiVO_4$, with and without the addition of a SnO_2 layer, measured in an electrolyte solution of 1.0 M KBi with 0.5 M of Na_2SO_3 as a hole scavenger (pH = 9) at 1 kHz under dark conditions.

This proves its HBL capabilities, creating an increased charge separation and extraction potential, also seen in the cyclic voltammetry (Figure 4a) as a better fill factor. At 0.3 V_{RHE}, the effect is more pronounced, although the generated photocurrents are small at this potential, close to the flat-band condition. The higher HBL effect presented for the lowest applied potential can be explained by the fact that at equal applied potential, the sample with the SnO_2 layer has a more cathodic onset potential (Table 1), thus really having added extraction potential. All IPCE spectra for different voltages are presented in Figure S12, where a decrease of the total IPCE can be observed with more cathodic potentials, following the same trend as Figure 4a voltammetries.

Figure 6b compares the capacitance behavior of the 9-layer photoanodes, and as both samples have similar morphologies (Figure 2), thicknesses, and optical properties (Figure 3), it can be assumed that the differences between the two curves are due to the presence or absence of SnO_2. Both samples present a positive slope in the 0.3−0.4 V_{RHE} region (a sign of n-type semiconductors), a similar slope (doping level), and a clear shift to lower potentials when a SnO_2 layer is introduced, implying an extra space charge region is formed.

The flat-band potential (V_{fb}), the donor density (N_D), and the depletion region width (W) can be estimated by the analysis of the M−S measurements shown in Figure 6 and are presented in Table 2. High values of donor densities suggest that both photoanodes fabricated in this study are highly doped semiconductors.[29] Moreover, our samples present $W \leq$ photoanode thickness, which is desirable since the electric field generated in the depletion region will be maximum, enhancing the charge separation and extraction.[6] The presence of a SnO_2 layer induces a down-shift of 90 mV in the flat-band potential, similar to the ∼70 mV measured in the cyclic voltammetries (Table 1), improving charge separation and enhancing the fill factor and thus the overall performance of the photoanodes, as observed in Figure 4a.

Table 2. Parameters Obtained from the Mott−Schottky Plots of 9-Layer Samples (Figure 6)[a]

sample	V_{fb} (V_{RHE})	N_D (cm^{-3})	W (nm)
$BiVO_4$	0.25	2.9×10^{18}	34.8
$BiVO_4$ + SnO_2	0.16	3.1×10^{18}	38.9

[a]Flat-band potential (V_{fb}), donor density (N_D), and depletion region width (W).

CONCLUSIONS

$BiVO_4$ photoanodes were fabricated by the spin-coating method, varying the number of deposited layers and introducing a thin (<5 nm) SnO_2 hole-blocking layer. Spin-coating is proven capable of depositing thin films with minimal light scattering, which is ideal for tandem PEC/PV devices. Thicker samples increased the $BiVO_4$ grain size, simultaneously enhancing light absorption and generating larger photocurrents. The deposition process is found to deposit thicker $BiVO_4$ layers in the first coating cycle due to the filling of the FTO substrate's rugosity cavities, which is revealed by a larger IPCE per layer (IPCE/#L) ratio. SnO_2 intermediate <5 nm layer is found to smooth FTO's rugosity and to induce a 70−90 mV cathodic shift to the flat-band potential, acting as a hole-blocking layer and helping to achieve better fill factor of the photoanodes, without modifying the charge carrier density

https://doi.org/10.1021/acsaem.3c02775
ACS Appl. Energy Mater. 2024, 7, 1792−1801

in the $BiVO_4$. The SnO_2 intermediate layer was also found to enhance charge separation and extraction for the lower energetic wavelengths.

The APCE revealed that the internal photon conversion efficiency increases when thicker samples are fabricated, up to 31% in our case, a sign of better internal charge separation and extraction together with a slight reduction of the $BiVO_4$ effective band gap. Finding a linear dependency of the internal APCE conversion with film thickness is key to incorporating this parameter into the computational simulation of light propagation based on the transfer matrix method. This enabled accurate matching of the predicted IPCE with experimentally obtained measurements. This establishes a first approach method to obtain the sample thickness just by knowing its IPCE, accounting for variating internal APCE conversion. This states, for the first time, the correlation of the internal conversion efficiency of $BiVO_4$ photoanodes with the material thickness, paving the way for precise computational modeling of light conversion efficiency. These findings establish a robust foundation for simulating tandem PV/PEC structures, fast-tracking the development of bias-free synthetic solar fuel devices.

■ ASSOCIATED CONTENT

Supporting Information

The Supporting Information is available free of charge at https://pubs.acs.org/doi/10.1021/acsaem.3c02775.

UV−vis transmittance and reflectance spectra, cyclic voltammetries, IPCE, and APCE supporting images are supplied in an additional document (PDF)

■ AUTHOR INFORMATION

Corresponding Author

Carles Ros − *ICFO - Institut de Ciencies Fotoniques, The Barcelona Institute of Science and Technology, 08860 Castelldefels, Spain;* orcid.org/0000-0002-9148-2767; Phone: (34) 935 53 40 02; Email: carles.ros@icfo.eu

Authors

Laura Geronimo − *ICFO - Institut de Ciencies Fotoniques, The Barcelona Institute of Science and Technology, 08860 Castelldefels, Spain*

Catarina G. Ferreira − *ICFO - Institut de Ciencies Fotoniques, The Barcelona Institute of Science and Technology, 08860 Castelldefels, Spain;* orcid.org/0000-0002-4088-1952

Valentina Gacha − *ICFO - Institut de Ciencies Fotoniques, The Barcelona Institute of Science and Technology, 08860 Castelldefels, Spain*

Dimitrios Raptis − *ICFO - Institut de Ciencies Fotoniques, The Barcelona Institute of Science and Technology, 08860 Castelldefels, Spain*

Jordi Martorell − *ICFO - Institut de Ciencies Fotoniques, The Barcelona Institute of Science and Technology, 08860 Castelldefels, Spain; Departament de Física, Universitat Politècnica de Catalunya, 08222 Terrassa, Spain*

Complete contact information is available at: https://pubs.acs.org/10.1021/acsaem.3c02775

Author Contributions

The manuscript was written through the contributions of all authors. All authors have approved the final version of the manuscript.

Notes

The authors declare no competing financial interest.

■ ACKNOWLEDGMENTS

ICFO acknowledges financial support from the LICROX and SOREC2 EU-funded projects (Codes: 951843 and 101084326), the BIST Program, and the Severo Ochoa Program. This work was partially funded by the CEX2019-000910-S (MCIN/AEI/10.13039/501100011033 and PID2020-112650RB-I00), Fundació Cellex, Fundació Mir-Puig, and Generalitat de Catalunya through CERCA. C.R. acknowledges support from the MCIN/AEI JdC-F Fellowship (FJC2020-043223-I) and the Severo Ochoa Excellence Postdoctoral Fellowship (CEX2019-000910-S).

■ REFERENCES

(1) Alami, A. H.; Rabaia, M. K. H.; Sayed, E. T.; Ramadan, M.; Abdelkareem, M. A.; Alasad, S.; Olabi, A. G. Management of Potential Challenges of PV Technology Proliferation. *Sustainable Energy Technol. Assess.* **2022**, *51*, No. 101942, DOI: 10.1016/j.seta.2021.101942.

(2) Polman, A.; Knight, M.; Garnett, E. C.; Ehrler, B.; Sinke, W. C.; Summary, R.; Polman, A.; Knight, M.; Garnett, E. C.; Ehrler, B.; Sinke, W. C. Photovoltaic Materials − Present Efficiencies and Future Challenges. *Science* **2016**, *352* (6283), 307.

(3) Ueckerdt, F.; Bauer, C.; Dirnaichner, A.; Everall, J.; Sacchi, R.; Luderer, G. Potential and Risks of Hydrogen-Based e-Fuels in Climate Change Mitigation. *Nat. Clim. Change* **2021**, *11* (5), 384−393.

(4) Ros, C.; Andreu, T.; Morante, J. R. Photoelectrochemical Water Splitting: A Road from Stable Metal Oxides to Protected Thin Film Solar Cells. *J. Mater. Chem. A* **2020**, *8*, 10625−10669.

(5) Fujishima, A.; Honda, K. Electrochemical Photolysis of Water at a Semiconductor Electrode. *Nature* **1972**, *238* (5358), 37−38.

(6) Ros, C.; Fabrega, C.; Monllor-Satoca, D.; Hernández-Alonso, M. D.; Penelas-Pérez, G.; Morante, J. R.; Andreu, T. Hydrogenation and Structuration of TiO 2 Nanorods Photoanodes: Doping Level and the Effect of Illumination in Trap-States Filling. *J. Phys. Chem. C* **2018**, *122* (6), 3295−3304.

(7) Martins, P. M.; Ferreira, C. G.; Silva, A. R.; Magalhães, B.; Alves, M. M.; Pereira, L.; Marques, P. A. A. P.; Melle-Franco, M.; Lanceros-Méndez, S. TiO2/Graphene and TiO2/Graphene Oxide Nanocomposites for Photocatalytic Applications: A Computer Modeling and Experimental Study. *Compos. B Eng.* **2018**, *145* (November 2017), 39−46.

(8) Fàbrega, C.; Murcia-López, S.; Monllor-Satoca, D.; Prades, J. D.; Hernández-Alonso, M. D.; Penelas, G.; Morante, J. R.; Andreu, T. Efficient WO3 Photoanodes Fabricated by Pulsed Laser Deposition for Photoelectrochemical Water Splitting with High Faradaic Efficiency. *Appl. Catal., B* **2016**, *189*, 133−140.

(9) Tang, P.; Xie, H.; Ros, C.; Han, L.; Biset-Peiró, M.; He, Y.; Kramer, W.; Rodríguez, A. P.; Saucedo, E.; Galán-Mascarós, J. R.; Andreu, T.; Morante, J. R.; Arbiol, J. Enhanced Photoelectrochemical Water Splitting of Hematite Multilayer Nanowire Photoanodes by Tuning the Surface State via Bottom-up Interfacial Engineering. *Energy Environ. Sci.* **2017**, *10* (10), 2124−2136.

(10) Schleuning, M.; Kölbach, M.; Ahmet, I.; Präg, R.; Gottesman, R.; Gunder, R.; Zhang, M.; Wargulski, D. R.; Abou-Ras, D.; Grave, D. A.; Abdi, F. F.; van de Krol, R.; Schwarzburg, K.; Eichberger, R.; Friedrich, D.; Hempel, H. Carrier Localization on the Nanometer-Scale Limits Transport in Metal Oxide Photoabsorbers. *Adv. Funct. Mater.* **2023**, *33*, No. 2300065, DOI: 10.1002/adfm.202300065.

(11) Kim, J. H.; Lee, J. S. Elaborately Modified BiVO4 Photoanodes for Solar Water Splitting. *Adv. Mater.* **2019**, *31* (20), No. e1806938.

(12) Murcia-López, S.; Fàbrega, C.; Monllor-Satoca, D.; Hernández-Alonso, M. D.; Penelas-Pérez, G.; Morata, A.; Morante, J. R.; Andreu, T. Tailoring Multilayered BiVO4 Photoanodes by Pulsed Laser

Deposition for Water Splitting. *ACS Appl. Mater. Interfaces* **2016**, *8* (6), 4076−4085.
(13) Shi, Q.; Murcia-López, S.; Tang, P.; Flox, C.; Morante, J. R.; Bian, Z.; Wang, H.; Andreu, T. Role of Tungsten Doping on the Surface States in BiVO4 Photoanodes for Water Oxidation: Tuning the Electron Trapping Process. *ACS Catal.* **2018**, *8* (4), 3331−3342.
(14) Zachäus, C.; Abdi, F. F.; Peter, L. M.; Van De Krol, R. Photocurrent of BiVO4 Is Limited by Surface Recombination, Not Surface Catalysis. *Chem. Sci.* **2017**, *8* (5), 3712−3719.
(15) Biset-Peiró, M.; Fàbrega, C.; Morante, J. R.; Andreu, T.; Murcia-López, S.; Fàbrega, C.; Morante, J. R.; Andreu, T. Multilayer Ni/Fe Thin Films as Oxygen Evolution Catalysts for Solar Fuel Production. *J. Phys. D Appl. Phys.* **2017**, *50* (10), No. 104003.
(16) Kunzelmann, V. F.; Jiang, C.-M.; Ihrke, I.; Sirotti, E.; Rieth, T.; Henning, A.; Eichhorn, J.; Sharp, I. D. Solution-Based Synthesis of Wafer-Scale Epitaxial BiVO4 Thin Films Exhibiting High Structural and Optoelectronic Quality. *J. Mater. Chem. A* **2022**, *10*, 12026−12034, DOI: 10.1039/d1ta10732a.
(17) Holland, S. K.; Dutter, M. R.; Lawrence, D. J.; Reisner, B. A.; DeVore, T. C. Photoelectrochemical Performance of W-Doped BiVO4 Thin Films Deposited by Spray Pyrolysis. *J. Photonics Energy* **2014**, *4* (1), No. 041598.
(18) Tolod, K. R.; Hernández, S.; Castellino, M.; Deorsola, F. A.; Davarpanah, E.; Russo, N. Optimization of BiVO4 Photoelectrodes Made by Electrodeposition for Sun-Driven Water Oxidation. *Int. J. Hydrogen Energy* **2020**, *45* (1), 605−618.
(19) Baek, J. H.; Kim, B. J.; Han, G. S.; Hwang, S. W.; Kim, D. R.; Cho, I. S.; Jung, H. S. BiVO4/WO3/SnO2 Double-Heterojunction Photoanode with Enhanced Charge Separation and Visible-Transparency for Bias-Free Solar Water-Splitting with a Perovskite Solar Cell. *ACS Appl. Mater. Interfaces* **2017**, *9* (2), 1479−1487.
(20) Shi, L.; Zhuo, S.; Abulikemu, M.; Mettela, G.; Palaniselvam, T.; Rasul, S.; Tang, B.; Yan, B.; Saleh, N. B.; Wang, P. Annealing Temperature Effects on Photoelectrochemical Performance of Bismuth Vanadate Thin Film Photoelectrodes. *RSC Adv.* **2018**, *8* (51), 29179−29188.
(21) Byun, S.; Kim, B.; Jeon, S.; Shin, B. Effects of a SnO2 Hole Blocking Layer in a BiVO4-Based Photoanode on Photoelectrocatalytic Water Oxidation. *J. Mater. Chem. A* **2017**, *5* (15), 6905−6913.
(22) Sivula, K.; Prevot, M. S. Photoelectrochemical Tandem Cells for Solar Water Splitting. *J. Phys. Chem. C* **2013**, *117*, 17879−17893.
(23) Ferreira, C. G.; Sansierra, C.; Bernal-Texca, F.; Zhang, M.; Ros, C.; Martorell, J. Bias-Free Solar-to-Hydrogen in a BiVO4/PM6:Y6 Compact Tandem with Optically Balanced Light Absorption. *Energy Environ. Mater.* **2023**, No. e12679.
(24) Kuang, Y.; Jia, Q.; Nishiyama, H.; Yamada, T.; Kudo, A.; Domen, K. A Front-Illuminated Nanostructured Transparent BiVO4 Photoanode for > 2% Efficient Water Splitting. *Adv. Energy Mater.* **2016**, *6* (2), 2−8.
(25) Kim, T. W.; Choi, K. S. Nanoporous BiVO4 Photoanodes with Dual-Layer Oxygen Evolution Catalysts for Solar Water Splitting. *Science* **2014**, *343* (6174), 990−994.
(26) Pihosh, Y.; Turkevych, I.; Mawatari, K.; Uemura, J.; Kazoe, Y.; Kosar, S.; Makita, K.; Sugaya, T.; Matsui, T.; Fujita, D.; Tosa, M.; Kondo, M.; Kitamori, T. Photocatalytic Generation of Hydrogen by Core-Shell WO3/BiVO4 Nanorods with Ultimate Water Splitting Efficiency. *Sci. Rep* **2015**, *5* (May), No. 11141.
(27) Tauc, J. Optical Properties and Electronic Structure of Amorphous Ge and Si. *Mater. Res. Bull.* **1968**, *3*, 37−46.
(28) Chen, Z.; Jaramillo, T. F.; Deutsch, T. G.; Kleiman-Shwarsctein, A.; Forman, A. J.; Gaillard, N.; Garland, R.; Takanabe, K.; Heske, C.; Sunkara, M.; McFarland, E. W.; Domen, K.; Miller, E. L.; Milled, E. L.; Turner, J. A.; Dinh, H. N. Accelerating Materials Development for Photoelectrochemical Hydrogen Production: Standards for Methods, Definitions, and Reporting Protocols. *J. Mater. Res.* **2010**, *25* (1), 3−16.
(29) Ravishankar, S.; Bisquert, J.; Kirchartz, T. Interpretation of Mott-Schottky Plots of Photoanodes for Water Splitting. *Chem. Sci.* **2022**, *13* (17), 4828−4837.
(30) Arunachalam, M.; Yun, G.; Lee, H. S.; Ahn, K. S.; Heo, J.; Kang, S. H. Effects of Al2O3 Coating on BIVO4and MO-Doped BIVO4 Film for Solar Water Oxidation. *J. Electrochem. Sci. Technol.* **2019**, *10* (4), 424−432.
(31) Kramarenko, M.; Ferreira, C. G.; Martínez-Denegri, G.; Sansierra, C.; Toudert, J.; Martorell, J. Relation between Fluorescence Quantum Yield and Open-Circuit Voltage in Complete Perovskite Solar Cells. *Solar RRL* **2020**, *4* (4), No. 1900554, DOI: 10.1002/solr.201900554.
(32) Persson, N. K.; Arwin, H.; Inganas, O. Optical Optimization of Polyfluorene-Fullerene Blend Photodiodes. *J. Appl. Phys.* **2005**, *97* (3), No. 034503, DOI: 10.1063/1.1836005.
(33) Kahng, S.; Kim, J. H. Heterojunction Photoanode of SnO2 and Mo-Doped BiVO4 for Boosting Photoelectrochemical Performance and Tetracycline Hydrochloride Degradation. *Chemosphere* **2022**, *291*, No. 132800.
(34) Song, J.; Seo, M. J.; Lee, T. H.; Jo, Y. R.; Lee, J.; Kim, T. L.; Kim, S. Y.; Kim, S. M.; Jeong, S. Y.; An, H.; Kim, S.; Lee, B. H.; Lee, D.; Jang, H. W.; Kim, B. J.; Lee, S. Tailoring Crystallographic Orientations to Substantially Enhance Charge Separation Efficiency in Anisotropic BiVO4 Photoanodes. *ACS Catal.* **2018**, *8* (7), 5952−5962.
(35) Lamers, M.; Li, W.; Favaro, M.; Starr, D. E.; Friedrich, D.; Lardhi, S.; Cavallo, L.; Harb, M.; Van De Krol, R.; Wong, L. H.; Abdi, F. F. Enhanced Carrier Transport and Bandgap Reduction in Sulfur-Modified BiVO4 Photoanodes. *Chem. Mater.* **2018**, *30* (23), 8630−8638.
(36) Cooper, J. K.; Gul, S.; Toma, F. M.; Chen, L.; Liu, Y. S.; Guo, J.; Ager, J. W.; Yano, J.; Sharp, I. D. Indirect Bandgap and Optical Properties of Monoclinic Bismuth Vanadate. *J. Phys. Chem. C* **2015**, *119* (6), 2969−2974.
(37) Gong, H.; Freudenberg, N.; Nie, M.; Van De Krol, R.; Ellmer, K. BiVO4 Photoanodes for Water Splitting with High Injection Efficiency, Deposited by Reactive Magnetron Co-Sputtering. *AIP Adv.* **2016**, *6* (4), No. 045108, DOI: 10.1063/1.4947121.
(38) Lopes, O. F.; Carvalho, K. T. G.; Nogueira, A. E.; Avansi, W.; Ribeiro, C. Controlled Synthesis of BiVO4 Photocatalysts: Evidence of the Role of Heterojunctions in Their Catalytic Performance Driven by Visible-Light. *Appl. Catal., B* **2016**, *188*, 87−97.
(39) Polo, A.; Dozzi, M. V.; Grigioni, I.; Lhermitte, C.; Plainpan, N.; Moretti, L.; Cerullo, G.; Sivula, K.; Selli, E. Multiple Effects Induced by Mo6+ Doping in BiVO4 Photoanodes. *Solar RRL* **2022**, *6* (9), No. 2200349, DOI: 10.1002/solr.202200349.
(40) Kosar, S.; Pihosh, Y.; Bekarevich, R.; Mitsuishi, K.; Mawatari, K.; Kazoe, Y.; Kitamori, T.; Tosa, M.; Tarasov, A. B.; Goodilin, E. A.; Struk, Y. M.; Kondo, M.; Turkevych, I. Highly Efficient Photocatalytic Conversion of Solar Energy to Hydrogen by WO3/BiVO4 Core−Shell Heterojunction Nanorods. *Appl. Nanosci.* **2019**, *9* (5), 1017−1024.
(41) Wohlgemuth, J. H.*Standards for PV Modules and Components-Recent Developments and Challenges Preprint STANDARDS FOR PV MODULES AND COMPONENTS-RECENT DEVELOPMENTS AND CHALLENGES*; 2012. http://www.osti.gov/bridge.
(42) Zhu, B. L.; Liu, F.; Li, K.; Lv, K.; Wu, J.; Gan, Z. H.; Liu, J.; Zeng, D. W.; Xie, C. S. Sputtering Deposition of Transparent Conductive F-Doped SnO2 (FTO) Thin Films in Hydrogen-Containing Atmosphere. *Ceram. Int.* **2017**, *43* (13), 10288−10298.